

A New Fick-Jacobs Derivation with Applications to Computational Branched Diffusion Networks

Zachary M. Miksis* Gillian Queisser*

May 23, 2025

Abstract

The Fick-Jacobs equation is a classical model reduction of 3-dimensional diffusion in a tube of varying radius to a 1-dimensional problem with radially scaled derivatives. This model has been shown to be unstable when the radial gradient is too steep. In this work, we present a new derivation of the Fick-Jacobs equation that results in the addition of higher order spatial derivative terms that provide additional stability in a wide variety of cases and improved solution convergence. We also derive new numerical schemes for branched nodes within networks and provide stability conditions for these schemes. The computational accuracy, efficiency, and stability of our method is demonstrated through a variety of numerical examples.

1 Introduction

Many biological, engineering, and experimental applications fundamentally rely on diffusion processes in bounded domains, particularly with porous boundaries. Among many others, such processes arise in ion transport through biological membranes [13, 29], carbon nanotubes [2], diffusion across a porous medium interface [1], biosensors [18], or permeation tubes [19]. For any application in which the domain geometry can affect the underlying (bio)physical processes it becomes necessary to incorporate the geometric features into the mathematical model. A straightforward way is to cast and solve the problem in the full three-dimensional domain. The examples mentioned above describe processes in channels, tubes, and tubular networks and many methods are available to computationally treat these types of problems accurately, including Monte Carlo simulations [26] and finite element based methods [11]. However, computational bottlenecks arise when discretizing large tubular network structures that introduce a very large number of degrees of freedom, as would happen, e.g., in structures present in the cardiovascular system or the brain. In three space dimensions, this becomes computationally expensive and simulations quickly become intractable.

To address the problem posed by computational costs, methods based on the Fick-Jacobs equation [15] are frequently proposed. This equation analytically considers the diffusion equation in a three-dimensional tube and reduces the model to a one-dimensional equation that respects the variable radius of the domain. Clearly, a model reduced in this way would open the door for spatially larger or temporally longer simulations. Unfortunately, Zwanzig demonstrated that this model may be unstable when the gradient of the radius is too large [30]. To extend the region of stability, he proposed a spatially adaptive diffusion coefficient based on the changing radius. Since then, other adaptive diffusion coefficients have been proposed [22, 17], as well as temporal corrections [16] and

*Department of Mathematics, Temple University, Philadelphia, Pennsylvania, USA (miksis@temple.edu, queisser@temple.edu)

the inclusion of biharmonic coefficients [9]. It has been noted that, while they improve on the stability of the classic Fick-Jacobs equation, many still present computational instabilities due to the radial gradient [4].

An additional complication arises in branching networks. While the previously mentioned methods are applicable to long tubes, they do not computationally address how to treat branching points in tubes that form a relatively large network. A common method for addressing this is via the Hines matrix [14] which is based on an indexing strategy of the network nodes. But this requires an additional reordering of the network done as a preconditioning step. A more direct method is to discretize the branch nodes in a way that respects conservation principles, as was done in [6] for diffusion problems.

In this paper, we propose a new and simplified derivation of the Fick-Jacobs model utilizing a high order expansion of the computed flux that, when applied in a discrete computational setting, produces second order spatial convergence and provides a much more accurate numerical solution at a wide range of radial gradients than previous correction methods. We also offer simple and computationally efficient discretizations of the various spatial derivatives at branching nodes, and provide stability conditions for these discretizations. The accuracy and stability of our method is demonstrated in numerical experiments.

Other methods for efficiently modeling these sorts of problems have been proposed, namely utilizing neural networks to decrease computational costs. These methods may often run into failings that inhibit their use in an applied setting: they may only contribute auxiliary information and therefore still require the solution of the PDE [12] as input, may sufficiently model the physics but lack the flexibility to model branched networks [20], or still require a complex numerical implementation to assist the network [21]. We will avoid these pitfalls by simplifying the numerical implementation while still keeping the fine grain information of the entire network.

The structure of the paper is as follows: in Section 2, we present the original derivation of the Fick-Jacobs model and introduce a modified derivation method that leads to our new model, termed Extended-Flux Fick-Jacobs (EF-FJ) model. In Section 3, we describe the one-dimensional spatial discretization methods we use for the different terms of our model, and how those discretizations are specialized for branch nodes in a one-dimensional network. In Section 4, we provide a stability analysis of our discretizations and prove new stability conditions on branching one-dimensional networks. Finally, in Section 5, we demonstrate that our method outperforms existing methods with respect to computational error, stability, and efficiency on multiple domains of changing radius, including a branched domain. Given the importance of the developed EF-FJ model to neuroscience we end with an example using a reconstructed neuron and simulate intracellular calcium dynamics inside the neuron.

2 Expanded Flux Fick-Jacobs Derivation

In this section, we present the derivation of the Fick-Jacobs equation from [15], and several of the major corrections made to both the spatial and temporal terms in recent decades. We then derive our expanded flux form of the Fick-Jacobs equation and distinguish this from previous derivations and corrections, which includes incorporating lateral fluxes in a simplified manner, and lay out the qualitative conservation conditions that must be satisfied at branch points in a network and incorporated into numerical methods.

2.1 Original Fick-Jacobs Derivation

In [15], Jacobs provided a derivation of a 1D reduced model of diffusion through a domain with varying radius. This was done by assuming radial and (horizontal) axial symmetry in an infinitesimal domain. This is shown visually in Fig. 1. Taking the total flux through the left face of the

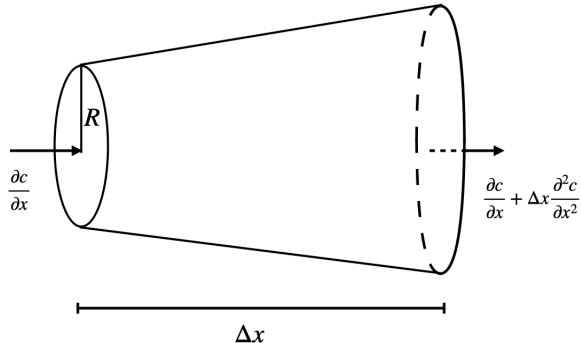


Figure 1: Jacobs flux through a truncated cone.

truncated cone and subtracting the total flux through the right face, we get the total flux through the domain. This is equal to the change in concentration in time over the whole volume of the domain. Setting these equal to each other and ignoring infinitesimal Δx terms, Jacobs derived what is now referred to as the Fick-Jacobs equation,

$$\frac{\partial c}{\partial t} = D_0 \left[\frac{\partial^2 c}{\partial x^2} + \frac{2}{R} \frac{dR}{dx} \frac{\partial c}{\partial x} \right], \quad (1)$$

where c denotes the concentration of some quantity of interest, D_0 the constant diffusion coefficient of c , and R the domain's cross-sectional radius, which depends on the axial direction x .

2.2 Diffusion Coefficient Correction

Different models have been proposed to modify the diffusion coefficient and improve results on steep domains [3]. Common ones include [30, 22, 17]:

$$D(x) = D_0 \quad (\text{Fick-Jacobs}) \quad (2)$$

$$D_{Zw}(x) = \frac{D_0}{1 + [R']^2/2} \quad (\text{Zwanzig}) \quad (3)$$

$$D_{RR}(x) = \frac{D_0}{(1 + [R']^2/4)^{1/3}} \quad (\text{Reguera-Rubi}) \quad (4)$$

$$D_{KP}(x) = \frac{D_0 \cdot \arctan([R']/2)}{[R']/2} \quad (\text{Kalinay-Percus}) \quad (5)$$

Here, we define $R' \equiv dR/dx$. Unlike our model presented in Sec. 2.4, these are mainly developed by different methods of deriving and analyzing the Fick-Jacobs equation from the Smoluchowski equation, which we do not detail here. This requires more analysis, but results in a continuous PDE that does not rely on Δx . We implement and numerically compare our expanded flux model to these corrections in later sections.

2.3 Kalinay Temporal Correction

Kalinay extended the Zwanzig derivation to add temporal correction terms similar to those we derive for our model in eq. (12), and demonstrated the improved effectiveness of this on a 2D cone [16]. Following the process described in the next section for 2D problems results in the original Fick-Jacobs equation without higher order terms, so we will not address here.

The Kalinay correction affects only the left side of the equation. It is done by setting the left hand side of the Fick-Jacobs equation to

$$[1 + \partial_x g(x)] \frac{\partial c}{\partial t}, \quad (6)$$

where, again letting $R' \equiv dR/dx$ and ϵ be some scaling term,

$$g(x) = \frac{x}{2} \left(\frac{\arctan \sqrt{\epsilon} R'}{\sqrt{\epsilon} R'} + \frac{\sqrt{\epsilon} R'}{3} \arctan \sqrt{\epsilon} R' - 1 \right). \quad (7)$$

It is assumed that $\epsilon = 1$ in all numerical tests, as in [16].

2.4 Expanded Flux Fick-Jacobs Equation

In contrast to the approaches taken in Sec. 2.1 – 2.3 we now consider the flux on both the left and the right side of the domain as expansions of the flux through the center of the domain, shown in Fig. 2.

2.4.1 Derivation of the Expanded Flux Fick-Jacobs equation

Using this reconsideration of the model, the flux from the left side of the truncated cone is

$$-D_0 \left(\pi \left(R - \frac{\Delta x}{2} \frac{dR}{dx} \right)^2 \right) \left(\frac{\partial c}{\partial x} - \frac{\Delta x}{2} \frac{\partial^2 c}{\partial x^2} + \frac{\Delta x^2}{8} \frac{\partial^3 c}{\partial x^3} - \dots \right),$$

and from the right

$$-D_0 \left(\pi \left(R + \frac{\Delta x}{2} \frac{dR}{dx} \right)^2 \right) \left(\frac{\partial c}{\partial x} + \frac{\Delta x}{2} \frac{\partial^2 c}{\partial x^2} + \frac{\Delta x^2}{8} \frac{\partial^3 c}{\partial x^3} + \dots \right).$$

Subtracting these, the right side of the diffusion equation becomes

$$D_0 \pi \left[R^2 \Delta x \frac{\partial^2 c}{\partial x^2} + 2 \Delta x R \frac{dR}{dx} \frac{\partial c}{\partial x} + \frac{\Delta x^3}{4} \left(\frac{dR}{dx} \right)^2 \frac{\partial^2 c}{\partial x^2} + \frac{\Delta x^3 R}{4} \frac{dR}{dx} \frac{\partial^3 c}{\partial x^3} + \dots \right] \quad (8)$$

For the left side of the equation, we similarly multiply the volume by the rate of change of concentration in time,

$$\frac{\Delta x}{3} \pi \left[\left(R - \frac{\Delta x}{2} \frac{dR}{dx} \right)^2 + \left(R + \frac{\Delta x}{2} \frac{dR}{dx} \right)^2 + \left(R - \frac{\Delta x}{2} \frac{dR}{dx} \right) \left(R + \frac{\Delta x}{2} \frac{dR}{dx} \right) \right] \frac{\partial c}{\partial t},$$

which simplifies to

$$\Delta x \pi \left[R^2 + \frac{\Delta x^2}{12} \left(\frac{dR}{dx} \right)^2 \right] \frac{\partial c}{\partial t}. \quad (9)$$

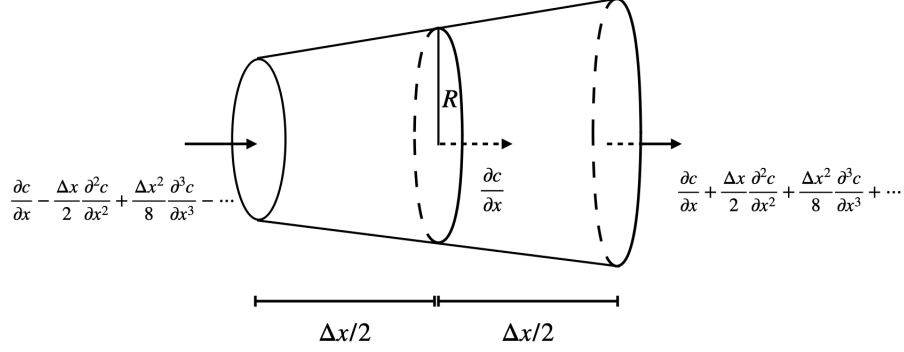


Figure 2: Expanded Jacobs flux through a truncated cone.

For the lateral surface flux, we take the locally averaged flux J in the middle of the domain, compute the total flux around the circumference, and integrate over the lateral surface of the domain. This gives us

$$2\pi \int_{-\frac{\Delta x}{2}}^{\frac{\Delta x}{2}} \left[R + s \frac{dR}{dx} \right] \left[J + s \frac{dJ}{dx} + \frac{s^2}{2} \frac{d^2 J}{dx^2} + \frac{s^3}{6} \frac{d^3 J}{dx^3} + \dots \right] ds. \quad (10)$$

Dropping higher order terms, integrating, and simplifying, we get an expansion for the lateral flux,

$$2\pi \left[\Delta x R J + \frac{\Delta x^3}{72} \left(6 \frac{dR}{dx} \frac{dJ}{dx} + 3R \frac{d^2 J}{dx^2} + R \frac{d^3 J}{dx^3} \right) \right]. \quad (11)$$

Setting the terms equal to each other, dividing by $\pi \Delta x R^2$, and dropping unwritten higher order expansion terms for practical implementation (these terms may be added in from the expansions above if a specific application necessitates them) gives the expanded flux Fick-Jacobs equation,

$$\begin{aligned} \left[1 + \frac{\Delta x^2}{12R^2} \left(\frac{dR}{dx} \right)^2 \right] \frac{\partial c}{\partial t} &= D_0 \left[\frac{\partial^2 c}{\partial x^2} + \frac{2}{R} \frac{dR}{dx} \frac{\partial c}{\partial x} + \frac{\Delta x^2}{4R} \frac{dR}{dx} \left(\frac{1}{R} \frac{dR}{dx} \frac{\partial^2 c}{\partial x^2} + \frac{\partial^3 c}{\partial x^3} \right) \right] \\ &+ \left[\frac{2}{R} J + \frac{\Delta x^2}{12R} \left(\frac{2}{R} \frac{dR}{dx} \frac{dJ}{dx} + \frac{d^2 J}{dx^2} + \frac{1}{3} \frac{d^3 J}{dx^3} \right) \right]. \end{aligned} \quad (12)$$

Remark 1. *It should be noted that for the concentration c for large Δx and after dividing by the temporal correction term, the first order derivative term is roughly order $\mathcal{O}(\Delta x^{-2})$, while the second order expansion term is roughly order $\mathcal{O}(1)$. This means that, for large Δx , our model behaves similarly to a simple diffusion model (with a very slight correction from the roughly $\mathcal{O}(1)$ third order expansion term). We observe this effect in later sections.*

2.4.2 Branch Point Conservation Conditions

For branched network systems, we must take special care at branch points by making physically consistent assumptions that can be incorporated into the construction of the numerical schemes. In general, these are assumptions of conservation. Specifically,

1. *Diffusive conservation:* At all points in the domain, the total diffusive flux in is equal to the total diffusive flux out.
2. *Mass conservation:* At all points in the domain, there is a conservation of total concentration.

3 Numerical Methods

In this section, we describe the finite difference discretizations for each spatial derivative term in eq. (12). All terms are discretized using second order methods.

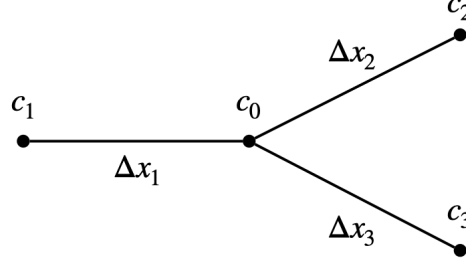


Figure 3: A discretized branch point of a network.

The first term we define is, naturally, the diffusion term. For the discretization shown in Fig. 3, we use a general central difference discretization for a branched structure, proposed in [5],

$$D \frac{\partial^2 c}{\partial x^2} \approx \frac{2D}{\sum_{1 \leq j \leq 3} \Delta x_j} \left(\sum_{1 \leq j \leq 3} \frac{c_j}{\Delta x_j} - c_0 \sum_{1 \leq j \leq 3} \frac{1}{\Delta x_j} \right), \quad (13)$$

which reduces to the standard central difference method on a cable. This method is second order accurate and conditionally stable, which we demonstrate in Sec. 4. In the case of using the additional third order expansion term, we compute this by simply taking a central difference of the diffusive term.

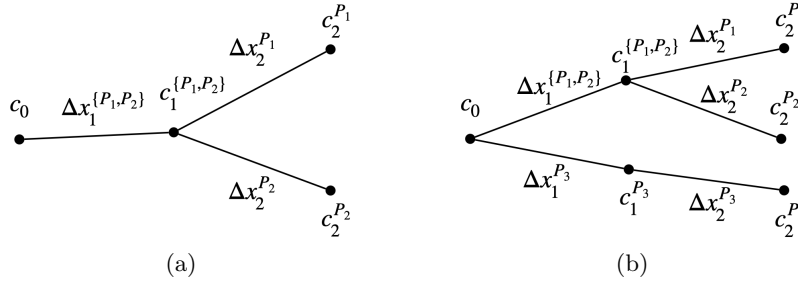


Figure 4: Possible branching 2-paths P_i with concentrations c_i .

For the first order term, we use second order upwinding. Here we must be careful, as this requires two nodes to the right (or left, depending on the "wind" direction), and branching can occur at any node in the network. To account for this, we consider all 2-paths, P_i , originating from our origin node. Fig. 4 shows two possible arrangements of these 2-paths. To approximate the first order term, we then take a linear combination of the derivatives along each 2-path:

$$D \frac{2}{R} \frac{dR}{dx} \frac{\partial c}{\partial x} \approx D \sum_{P_j \in S} \frac{2}{R} \frac{dR}{dx} \frac{1}{\Delta x_1 \Delta x_2 (\Delta x_1 + \Delta x_2)} \left(-\Delta x_1^2 c_2 + (\Delta x_1 + \Delta x_2)^2 c_1 - (2\Delta x_1 \Delta x_2 + \Delta x_2^2) c_0 \right). \quad (14)$$

Care is taken here when using the dR/dx term. When determining the "wind" direction, we compute dR/dx using *central differencing* at the origin node, but when computing each term of the summation, we compute dR/dx using *upwinding* along the particular 2-path. This distinction allows us to choose the appropriate direction to compute the derivative from, while accurately computing the derivative along each individual 2-path by excluding information from irrelevant edges and nodes.

3.1 Boundary Nodes

To compute higher order derivatives at the boundary nodes, we assume knowledge of Neumann boundary conditions and utilize this to ensure only interior nodes are required. This was done previously for the diffusion term in [5], so we will only show the third order term here. Define the node $i = 0$ as the boundary node, $i = -1$ as a ghost node to the left, and $i = 1, 2$ as the interior nodes to the right. We first start with Taylor expansions of c_{-1} and c_2 around node $i = 0$, under the assumption $\Delta x_i \equiv h$,

$$c_{-1} = c_0 - hc'_0 + \frac{h^2}{2}c''_0 - \frac{h^3}{6}c'''_0, \quad (15)$$

$$c_2 = c_0 + 2hc'_0 + 2h^2c''_0 + \frac{8h^3}{6}c'''_0. \quad (16)$$

These can be combined to remove the second derivative term,

$$c_2 - 4c_{-1} = -3c_0 + 6hc'_0 + 2h^3c'''_0 \quad (17)$$

Using a central difference approximation of the first derivative at node $i = 0$, we get an expression for c_{-1} ,

$$c_{-1} = c_1 - 2hc'_0$$

Substituting this into the previous equation and rearranging, we have

$$2h^3c'''_0 = c_2 + 3c_0 - 4(c_1 - 2hc'_0) - 6hc'_0,$$

or our full approximation

$$c'''_0 = \frac{c_2 - 4c_1 + 3c_0}{2h^3} + \frac{c'_0}{h^2}, \quad (18)$$

where c'_0 is given by Neumann boundary conditions. A similar derivation for c'''_n starting from expansions of c_{n-2} and c_{n+1} (with $i = n$ the boundary node, $i = n - 1, n - 2$ the interior nodes to the left, and $i = n + 1$ a ghost node to the right) gives

$$c'''_n = \frac{-3c_n + 4c_{n-1} - c_{n-2}}{2h^3} + \frac{c'_n}{h^2}. \quad (19)$$

4 Stability Analysis

We have presented numerical discretizations at branching nodes, but these are only useful for computational models if they are stable methods. In this section, we present two key results for ensuring numerical stability in examples in the next section, that the numerical discretizations of both the diffusion and first order terms at branching nodes are conditionally stable. These results allow us to implement stable methods in Sec. 5. We first present the condition and proof for the diffusion term, and then for the first order term.

Theorem 1 (Diffusion is stable at branch nodes). *Given the diffusion equation*

$$\frac{\partial c}{\partial t} = D \frac{\partial^2 c}{\partial x^2},$$

the second order branched forward-time central-space (FTCS) scheme

$$c_i^{n+1} = c_i^n + \frac{2D\Delta t}{\sum \Delta x_j} \left(\sum \frac{c_j^n}{\Delta x_j} - c_i^n \sum \frac{1}{\Delta x_j} \right)$$

is stable given the condition

$$\frac{D\Delta t}{\sum \Delta x_j} \cdot \sum \frac{1}{\Delta x_j} \leq \frac{1}{2}$$

is satisfied.

Proof. We demonstrate conditional stability of the second order FTCS scheme for branch nodes, such as the one shown in Fig. 3. Given the general FTCS method at branch nodes [6, 5]:

$$c_i^{n+1} = c_i^n + \frac{2D\Delta t}{\sum \Delta x_j} \left(\sum \frac{c_j^n}{\Delta x_j} - c_i^n \sum \frac{1}{\Delta x_j} \right),$$

and applying the Fourier transform,

$$\hat{c}^n(\xi) = \frac{1}{\sqrt{2\pi}} \sum_{k=-\infty}^{\infty} e^{-ik\xi} c_k^n$$

and the following fact [28],

$$\frac{1}{\sqrt{2\pi}} \sum_{k=-\infty}^{\infty} e^{-ik\xi} c_{k\pm 1}^n = e^{\pm i\xi} \hat{c}(\xi).$$

Define

$$\alpha = \frac{2D\Delta t}{\sum \Delta x_j}; \quad \beta = \sum \frac{1}{\Delta x_j}.$$

Using simplifying notation $\hat{c}^n := \hat{c}^n(\xi)$, at a branch point with edge Δx_1 to the left and edges Δx_2 , Δx_3 to the right, we have

$$\begin{aligned} \hat{c}^{n+1} &= \hat{c}^n + \alpha \left(\frac{1}{\Delta x_1} e^{-i\xi} \hat{c}^n + \frac{1}{\Delta x_2} e^{i\xi} \hat{c}^n + \frac{1}{\Delta x_3} e^{i\xi} \hat{c}^n - \beta \hat{c}^n \right) \\ &= \left[1 - \alpha\beta + \alpha \left(\frac{1}{\Delta x_1} e^{-i\xi} + \left(\frac{1}{\Delta x_2} + \frac{1}{\Delta x_3} \right) e^{i\xi} \right) \right] \hat{c}^n \\ &= \left[1 - \alpha\beta + \alpha \left(\frac{1}{\Delta x_1} e^{-i\xi} - \frac{1}{\Delta x_1} e^{i\xi} + \beta e^{i\xi} \right) \right] \hat{c}^n \\ &= \left[1 - \alpha\lambda + \alpha \left(\frac{-2i}{\Delta x_1} \sin(\xi) + \lambda e^{i\xi} \right) \right] \hat{c}^n \\ &= \left[1 - \alpha\beta + \alpha \left(\frac{-2i}{\Delta x_1} \sin(\xi) + \beta \cos(\xi) + i\beta \sin(\xi) \right) \right] \hat{c}^n \\ &= \left[1 + \alpha\beta(\cos(\xi) - 1) + i\alpha \left(\beta - \frac{2}{\Delta x_1} \right) \sin(\xi) \right] \hat{c}^n \\ &= \rho(\xi) \hat{c}^n \end{aligned}$$

For stability, we require $|\rho(\xi)| \leq 1$. We have

$$|\rho(\xi)|^2 = 1 + (\alpha\beta)^2[\cos(\xi) - 1]^2 + 2\alpha\beta[\cos(\xi) - 1] - \alpha^2 \left(\beta - \frac{2}{\Delta x_1} \right)^2 \sin^2(\xi).$$

Evaluating at $\xi = \pi$ gives the stability condition:

$$\begin{aligned} 1 + 4(\alpha\beta)^2 - 4\alpha\beta &\leq 1 \\ 4(\alpha\beta)^2 &\leq 4\alpha\beta \\ \alpha\beta &\leq 1 \end{aligned}$$

This condition is both necessary and sufficient. Expanded, the full condition is

$$\frac{D\Delta t}{\sum \Delta x_j} \cdot \sum \frac{1}{\Delta x_j} \leq \frac{1}{2}.$$

Given evenly spaced nodes, i.e., $\Delta x_j = \Delta x \forall j$, this reduces to the usual FTCS stability condition,

$$\frac{D\Delta t}{\Delta x^2} \leq \frac{1}{2}.$$

□

Theorem 2 (First order term is stable at branch nodes). *Given node x_0 with numerical concentration c_0 and set $S = \{P_1, P_2, \dots\}$ of 2-paths $P_i = \{x_0, x_1^{(P_i)}, x_2^{(P_i)}\}$ originating from x_0 with edge lengths $\{\Delta x_1, \Delta x_2\}$. Define the second order numerical upwind derivative as*

$$c'_0 = \sum_{P_j \in S} r \sum_{i=0}^2 A_i c_i,$$

where

$$r = \frac{1}{\Delta x_1 \Delta x_2 (\Delta x_1 + \Delta x_2)};$$

$$A_0 = -(2\Delta x_1 \Delta x_2 + \Delta x_2^2), \quad A_1 = (\Delta x_1 + \Delta x_2)^2, \quad A_2 = -\Delta x_1^2.$$

Further, define

$$\hat{A}_i = \Delta t D \sum_{P_j \in S} \frac{2}{R^{(P_j)}} \frac{dR^{(P_j)}}{dx} r A_i^{(P_j)},$$

where $R^{(P_j)}$ and $(dR/dx)^{(P_j)}$ are the cross-sectional radius and radial derivative at x_0 along path P_j , respectively. Then given the first order PDE

$$\frac{\partial c}{\partial t} = D \frac{2}{R} \frac{dR}{dx} \frac{\partial c}{\partial x},$$

the forward-time second order upwind method

$$c_0^{(n+1)} = c_0^{(n)} + \Delta t D \frac{2}{R} \frac{dR}{dx} c'_0$$

is stable, given the condition

$$\left| 1 + \hat{A}_0 - \hat{A}_1 + \hat{A}_2 \right| \leq 1$$

is satisfied.

Proof. Begin by defining the complete forward-time upwind method as

$$c_0^{(n+1)} = c_0^{(n)} + \Delta t D \sum_{P_j \in S} \frac{2}{R} \frac{dR}{dx} \frac{1}{\Delta x_1 \Delta x_2 (\Delta x_1 + \Delta x_2)} \left(-\Delta x_1^2 c_2 + (\Delta x_1 + \Delta x_2)^2 c_1 - (2\Delta x_1 \Delta x_2 + \Delta x_2^2) c_0 \right),$$

where all terms in the summation are understood to be taken at time step n and with respect to path P_j . Using the notation defined above, this may be simplified to

$$c_0^{(n+1)} = c_0^{(n)} + \Delta t D \sum_{P_j \in S} \frac{2}{R} \frac{dR}{dx} r (A_2 c_2 + A_1 c_1 + A_0 c_0).$$

Taking the Fourier transform of each side, we have

$$\begin{aligned} \hat{c}^{(n+1)} &= \hat{c}^{(n)} \left[1 + \Delta t D \sum_{P_j \in S} \frac{2}{R} \frac{dR}{dx} r \left(A_2 e^{2i\xi} + A_1 e^{i\xi} + A_0 \right) \right] \\ &= \hat{c}^{(n)} \left[1 + \Delta t D \sum_{P_j \in S} \frac{2}{R} \frac{dR}{dx} r \left(A_2 (\cos(2\xi) + i \sin(2\xi)) + A_1 (\cos(\xi) + i \sin(\xi)) + A_0 \right) \right] \\ &= \hat{c}^{(n)} \left[1 + \Delta t D \sum_{P_j \in S} \frac{2}{R} \frac{dR}{dx} r \left(A_2 (\cos^2(\xi) - \sin^2(\xi) + 2i \cos(\xi) \sin(\xi)) + A_1 (\cos(\xi) + i \sin(\xi)) + A_0 \right) \right] \\ &= \hat{c}^{(n)} \left[1 + \hat{A}_2 (\cos^2(\xi) - \sin^2(\xi) + 2i \cos(\xi) \sin(\xi)) + \hat{A}_1 (\cos(\xi) + i \sin(\xi)) + \hat{A}_0 \right] \end{aligned}$$

This gives us the sign

$$\rho(\xi) = 1 + \hat{A}_2 (\cos^2(\xi) - \sin^2(\xi) + 2i \cos(\xi) \sin(\xi)) + \hat{A}_1 (\cos(\xi) + i \sin(\xi)) + \hat{A}_0$$

We require that $|\rho(\xi)| \leq 1$ for stability. Taking $|\rho(\xi)|^2$ and evaluating at the maximum $\xi = \pi$, we arrive at the necessary stability condition

$$\left| 1 + \hat{A}_0 - \hat{A}_1 + \hat{A}_2 \right| \leq 1.$$

□

5 Numerical Results

Our model is derived by computing the spatially averaged local concentration, but other corrections were derived using the integral form of the Fick-Jacobs equation [30],

$$\frac{\partial G}{\partial t} = D_0 \frac{\partial}{\partial x} A(x) \frac{\partial}{\partial x} \frac{G}{A(x)}, \quad (20)$$

where $G(x, t)$ is the integral of local concentration $c(x, t)$. This form is conservative, but rather difficult to implement Neumann boundary conditions with. The expanded form is relatively simple to implement Neumann boundary conditions with, but is not conservative. Therefore, we will use eq. (1), the local form of the Fick-Jacobs equation, for evaluating the corrections from the literature.

Given an exact solution G and a numerical solution \widehat{G} over N spatial grid points x_i at time t_j , the L^1 error is computed as

$$\|G - \widehat{G}\|_1 = \frac{1}{N} \sum_{i=1}^N \left| \frac{G(x_i, t_j) - \widehat{G}_i^j}{G(x_i, t_j)} \right| \quad (21)$$

For computing of errors, we multiply the computed average local concentration by the area of the cross-sectional disk.

Throughout this section, we compare our expanded flux model (EF-FJ) with the original Fick-Jacobs model (FJ) and the Zwanzig (Zw), Reguera-Rubi (RR), Kalinay-Percus (KP), and Kalinay (Kal) corrections. Python code and geometry files for examples in this section is publicly available through GitHub¹.

5.1 Truncated Cone

We simulate diffusion through a truncated cone with a Gaussian initial condition [23]. Given a cross sectional area of $A(x) = \pi(1 + \lambda x)^2$ and the initial condition

$$G(x, 0) = \frac{1 + \lambda x}{(2\pi\sigma^2)^{1/2}} e^{-\frac{(x-a_0)^2}{4\sigma^2}}, \quad (22)$$

we have the exact solution

$$G(x, t) = (1 + \lambda x) \left(\frac{\sigma^2}{2\pi} \right)^{1/4} \frac{1}{(\sigma^2 + D_0 t)^{1/2}} e^{-\frac{x-a_0}{4(\sigma^2 + D_0 t)}}. \quad (23)$$

This allows us to prescribe Neumann conditions of the derivative of the exact solution at the ends of our computational domain.

For this example, we will use this exact solution to demonstrate the improvement in error that our model provides. For all computations, we use $\sigma = 4$, $a_0 = 0$, $D_0 = 1$, $\Delta t = 2 \times 10^{-4}$, and take the spatial grid $x \in [0, 10]$. The parameters λ and N vary by test. Note, the value λ determines the degree of tapering present in the network structure, i.e., small λ represent geometries closer to cylinders, while large values represent different degrees of truncated cone tapers.

5.1.1 Results

In Table 1, we present the computed L^1 errors at $t = 10$ for each model and correction. While the corrections were derived analytically to improve on the Fick-Jacobs model, we see from these results that the Fick-Jacobs model outperforms the corrections in practice. This was not observed in any of the existing literature, as the corrections were not previously implemented and compared directly with the Fick-Jacobs model.

Additionally, we see that our expanded flux model outperforms even the Fick-Jacobs model, while outperforming the corrections by an order of magnitude for $\lambda = 5$ and several orders of magnitude for $\lambda = 0.2$. The Fick-Jacobs model performs similarly well as our model for small λ , but for larger λ , our expanded flux model outperforms the Fick-Jacobs model by a factor of two. It becomes clear that, for both large and small λ , our model appears to be the best choice.

In Fig. 5, we have plotted each model and correction solution against the exact solution. We see that, as λ increases, more of the correction solutions move further and further away from the true solution, while our expanded flux model remains visually similar to the true solution. This visual confirmation of what we observed in Table 1 further demonstrates the effectiveness of our model.

¹<https://github.com/zmiksis/FJExpansion>

Table 1: L^1 errors at time $t = 10$ of different models for different values of λ .

λ	Model					
	EF-FJ	FJ	Zw	RR	KP	Kal
0.2	8.24E-6	9.74E-6	6.25E-4	1.07E-4	1.08E-4	6.29E-3
1	1.24E-3	1.70E-3	3.06E-2	6.31E-3	6.39E-3	1.25E-1
5	3.29E-2	6.29E-2	5.31E-1	2.19E-1	2.41E-1	6.01E-1

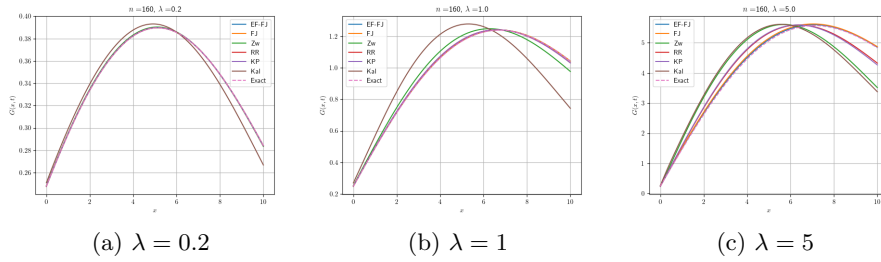


Figure 5: Numerical approximations by different models with exact solution at $t = 10$ in a truncated cone.

5.1.2 Temporal Stability

In Fig. 6, we show the error in the computed solution over time for each model and correction, now from $t = 0$ to $t = 100$. We see that, while there are a few “bumps” in the correction errors around $t = 10$, the models are temporally stable. Our model consistently produces the lowest error over time, remaining parallel to the error of the other models. This demonstrates that our model is stable for long time simulations, and will consistently produce the most accurate solution.

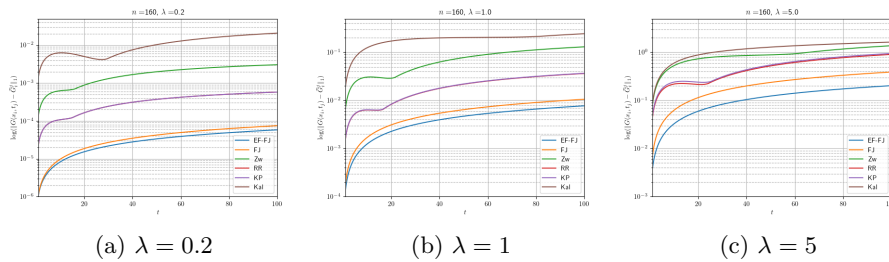


Figure 6: L^1 error of different models over time in a truncated cone.

5.1.3 Convergence

In Fig. 7 we present the spatial convergence for each model and correction. When λ is small (and the domain is nearly close to a straight tube), our model is parallel to the Fick-Jacobs model and demonstrates near perfect second order convergence. On the other hand, the corrections do not appear to converge at all, or they show limited convergence. Once again, our model is the best performing.

As λ gets larger, we begin to see larger errors in our model for larger values of Δx . This is due to Remark 1: for larger Δx , our model behaves more like a simple diffusion model. This was not an

issue with small λ because the radial derivative was small enough that the solution was very similar to a simple diffusion solution, but this is no longer the case for larger λ . The issue is corrected when Δx is sufficiently refined, and in both cases we see roughly second order convergence from both our method and the Fick-Jacobs method. Again, we see no or limited convergence from the corrections and with sufficiently small Δx , our model shows the best performance.

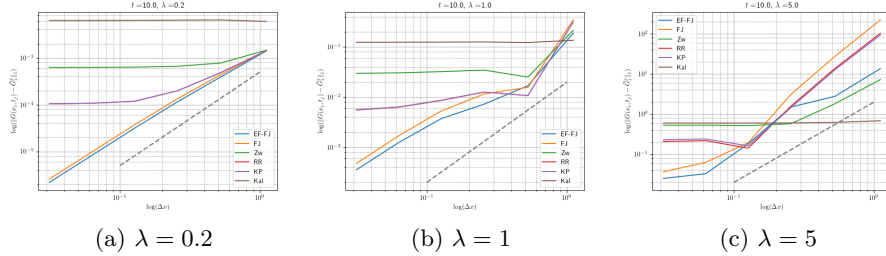


Figure 7: Convergence errors of different models at $t = 10$. Dashed line represents $O(\Delta x^2)$ convergence slope.

5.2 Sinusoidal Channel

We simulate diffusion through a sinusoidal with a Gaussian initial condition [23]. Given a cross sectional area of $A(x) = \sin^2 \gamma x$ and the initial condition

$$G(x, 0) = \frac{\sin(\gamma x)}{(2\pi\sigma^2)^{1/2}} e^{-\frac{(x-a_0)^2}{4\sigma^2}}, \quad (24)$$

we have the exact solution

$$G(x, t) = e^{D_0\gamma^2 t} \sin(\gamma x) \left(\frac{\sigma^2}{2\pi}\right)^{1/4} \frac{1}{(\sigma^2 + D_0 t)^{1/2}} e^{-\frac{x-a_0)^2}{4(\sigma^2 + D_0 t)}}. \quad (25)$$

This again allows us to prescribe Neumann conditions of the derivative of the exact solution at the ends of our computational domain.

For this example, we will use this exact solution to demonstrate the improvement in error that our model provides. For all computations, we use $\sigma = 2$, $a_0 = 1$, $D_0 = 1$, $\Delta t = 2 \times 10^{-4}$, and take $N = 160$ grid points over the spatial grid $x \in [1, \pi/\gamma - 1]$ and let γ vary.

The L^1 errors are shown in Table 2. We see that our model produces the most accurate solution out of all methods, nearly halving the error of the Fick-Jacobs method for larger γ values. Even with a nonconstant radial derivative, we have demonstrated that our method maintains a low error, and in some cases is several orders of magnitude less than the correction errors.

Table 2: L^1 errors at time $t = 10$ of different models for different values of γ for a sinusoidal channel.

γ	Model					
	EF-FJ	FJ	Zw	RR	KP	Kal
0.05	8.00E-5	1.09E-4	1.07E-4	1.09E-4	1.09E-4	1.07E-4
0.1	1.75E-4	3.24E-4	2.74E-4	3.15E-4	3.15E-4	2.74E-4
0.5	7.74E-4	1.25E-3	1.20E-1	1.97E-2	1.97E-2	1.22E-1

5.3 Branched Domain

We present results of diffusion on a branched network of varying radius. In Fig. 8a, we see the varying radius of the domain. On the left, we have a large entrance that quickly reduces to a small tube. On the two right endpoints, we expand into to larger exits from the domain, making sure we have both expanding and contracting radii. For this example, we keep $D_0 = 1$, but now have an inflow condition on left endpoint and an outflow condition on the two right endpoints such that the total inflow is equal to the total outflow.

In Fig. 8a, we show a model of the branched domain. We see that for most of the domain the radius does not vary much (small dR/dx), but there is a significant expansion at the left boundary (similar to a ball on a stick). On the two right boundaries, the radius ceases decreasing and increases instead, to demonstrate the effectiveness of our method on a branched domain that has both increasing and decreasing radius.

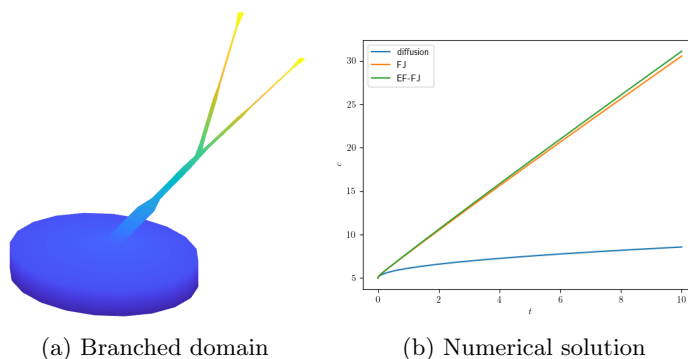


Figure 8: The (a) 3D rendering of the branched domain, and (b) numerical solution at the large endpoint of a branched domain using a simple diffusion model, the classical Fick-Jacobs model, and our expanded flux model.

We run the computation to a final unitless time of $t = 10$, and plot the solution at the left endpoint of the domain of our expanded flux method, the Fick-Jacobs model, and a simple diffusion model in Fig. 8b. We see that, as the influx is equal to the outflux, the simple diffusion model appears to behave as expected and approach a steady state. Alternatively, when the radius is taken into account in our model and the Fick-Jacobs model, we see that the concentration at the end node (the “ball”) is backed up and continues to increase, as it has trouble moving into the much smaller radius of the “stick”.

Further, in Fig. 9, we show the modeled concentration at $t = 0, 5$, and 10 using a simple diffusion model, the Fick-Jacobs model, and our expanded flux model. We see that the simple diffusion model does not change much, approaching its steady state, but the radius respecting models have a significant buildup of concentration in the “ball” and a depletion in the ends of the “stick”, where the inflow concentration is not able to diffuse quickly due to the quick reduction in radius size. Visually, these two models appear to behave similarly and as might be expected.

5.3.1 Convergence Analysis

For the Fick-Jacobs and expanded flux models, we observe convergence of the solution as we spatially refine the domain. In Fig. 10, we show the computed solution at the left end node for no refinement and four levels of refinement for each method. For the Fick-Jacobs method, we see

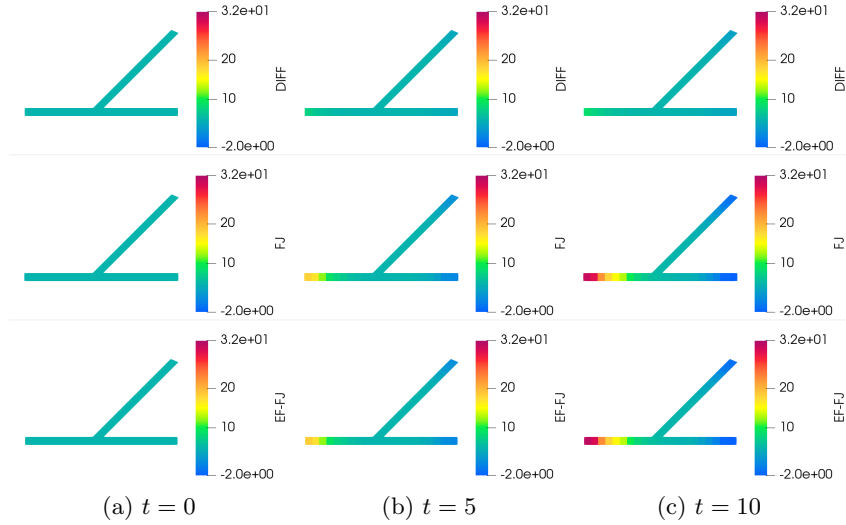


Figure 9: Numerical solution on a branched domain at $t = 0, 5,$ and $10,$ using a pure diffusion model, the classical Fick-Jacobs model, and our expanded flux model.

an initially steep slope of the increasing concentration, and that line slowly rising as the grid is refined. For the expanded flux method, we see an initial line that has a very shallow slope, nearing the shape of the simple diffusion model in Fig. 8b. This is due again to Remark 1: with a large $\Delta x,$ our model will behave similarly to a simple diffusion model, which we see here. However, unlike the Fick-Jacobs model, ours converges very quickly - the final two refinement levels are on essentially on top of each other, and are visually indistinguishable.

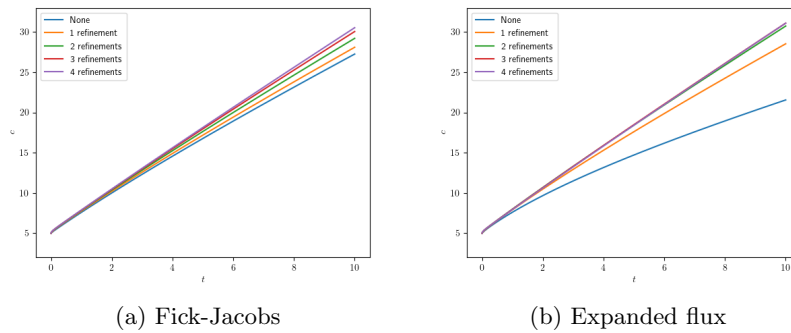


Figure 10: Converging numerical solutions at the left endpoint of a branched domain with different levels of spatial refinement using (a) the classical Fick-Jacobs model and (b) our expanded flux model.

To further observe convergence, we look at the relative numerical error. Due to our method converging visually so quickly (Fig. 10) and our solution lying above the Fick-Jacobs solution (Fig. 8b), we use our most refined solution as the reference solution. We then compute the relative L^1 errors, and report the errors in Fig. 11. From this figure, we see that not only is our solution converging faster, but it produces the smaller error. At all levels with sufficiently small Δx to avoid the diffusion dominance in the expanded flux method, the Fick-Jacobs method requires at least

twice the number of nodes as the expanded flux method to produce the same level of error. It is evident, both visually and numerically, that our expanded flux method converges sufficiently with just a few refinement levels, and that it converges significantly faster than the Fick-Jacobs method to a true solution.

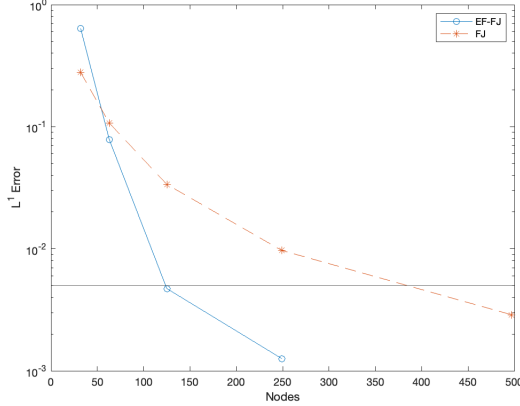


Figure 11: Relative L^1 error at different refinement levels at $t = 10$ for our expanded flux model and the classical Fick-Jacobs model.

Additionally, Fig. 11 shows a horizontal line for a relative error tolerance of 5×10^{-3} . We see from the figure that our method reaches this tolerance with a little more than 100 nodes, while the Fick-Jacobs method will require four times that number of nodes to reach the same tolerance. Given a required accuracy tolerance, our method will require much fewer nodes, and subsequently a fraction of the computation time, as we will show in the next subsection.

5.3.2 Computational Efficiency

While our expanded flux method has additional higher order derivative terms that the Fick-Jacobs method does not have, each method can be computationally implemented as

$$\frac{\partial c}{\partial t} = D_X c, \quad (26)$$

where D_X is the sum of all spatial derivative discretization matrices. This matrix can be pre-computed for both methods, and therefore only a single matrix-vector multiplication needs to be carried out in each step. The expanded flux method requires only a minimal number of additional operations per time step per third order or higher expansion term to account for the additional boundary condition inclusion, which does not effect the computation time. Table 3 shows the computation time in seconds required for a single step of each method, and we see that these are roughly equivalent for each domain size. If we were to require a relative L^1 error of 3×10^{-3} , we can see from the table that it would take the Fick-Jacobs method roughly 3 times as long as the expanded flux method. If we tighten that restriction to a relative L^1 error of 5×10^{-3} , it would take the Fick-Jacobs method nearly 8 times as long as the expanded flux method. It is clear from these results that with sufficient spatial refinement to avoid diffusion dominance, the expanded flux method is by far the most computationally efficient method.

Table 3: Single forward Euler step time in seconds at different refinement levels at $t = 10$ for our expanded flux model and the classical Fick-Jacobs model.

Nodes	EF-FJ		FJ	
	Step Time (s)	Ratio	Step Time (s)	Ratio
32	3.28E-6	–	3.38E-6	–
63	3.91E-6	1.19	4.00E-6	1.18
125	6.32E-6	1.62	6.13E-6	1.53
249	1.49E-5	2.36	1.44E-5	2.35
497	4.57E-5	3.06	4.60E-5	3.19

5.4 Branched Domain with Lateral Flux

We next consider a branched domain with lateral fluxes. This is something the classical Fick-Jacobs model was not designed to do, evident from eq. (1) having no term for boundary fluxes. In Jacobs’s original derivation, a key assumption was no boundary fluxes. Here, we use our expanded flux model to incorporate these.

The main influx sits on three nodes equidistant from the center branch node, one node on each branch of the domain. These nodes have an influx in the period $0 \leq t \leq 3$. We also include constant outflow conditions at the two right endpoints. Additionally, we add constraint conditions on the concentration on every point in the domain to make the domain mirror more realistic settings. If the concentration went above a value of $c = 6$, an outflow condition was triggered. If it dropped below $c = 4$, a no boundary flux condition was enforced.

In Fig. 12, we show the concentration throughout the domain at various time steps. By $t = 2$, we see the region around the branch node already nearing peak allowable concentration, while the region near the two right endpoints is reaching minimum allowable concentration. From $t = 4$ onward, we see the concentration begin to diffuse outwards, moving out of the domain from the two right boundaries while only slightly affecting the region with the larger radius to the left.

In Fig. 13, we see the convergence of the solution under spatial refinement at the left endpoint of the domain and at the branch node. At the base grid (no refinement), we see the diffusion dominant behavior as observed in previous examples. Under further refinement, we see the solution approaching a slow increase at the left endpoint, and smoothing out to a hill at the branch node. Once again, even with the lateral flux terms included, we confirm convergence of our numerical solution.

5.5 An application to neuroscience

Lastly, we consider a neuron and the calcium dynamics in response to synaptic stimuli, which is mathematically modeled as diffusion through a tubular network. Calcium dynamics in neurons are important for the study of treatments for various neurological conditions, as calcium acts as a messenger in neurons, regulating processes such as neurotransmitter release, synaptic plasticity, neuronal excitability, and regulation of DNA transcription. Biologists and neuroscientists rely on accurate simulations to conduct reliable analysis and develop effective treatments. For this reason, we provide this as an essential application of our model.

We compare the results of our model to those of a simplified version of the model for calcium

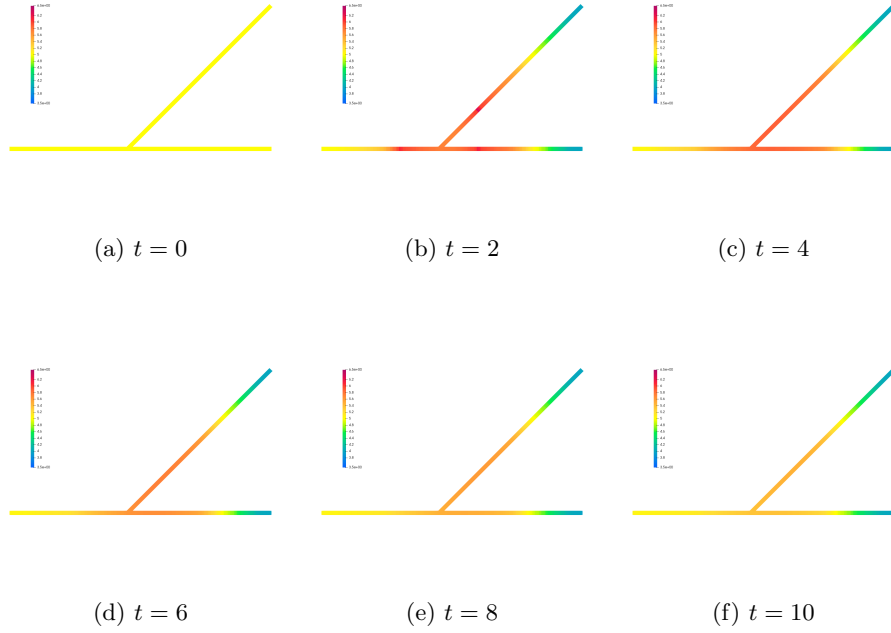


Figure 12: Numerical solutions on a branched domain with lateral influx and outflux at various values of t .

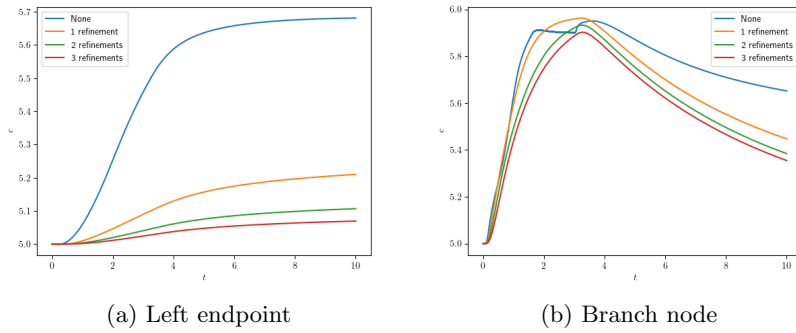


Figure 13: Converging numerical solutions of a branched domain with lateral flux at different levels of spatial refinement at (a) the left endpoint and (b) the branch node of the domain.

dynamics in [6],

$$\frac{\partial c}{\partial t} = \frac{\partial}{\partial x} \left(D \frac{\partial c}{\partial x} \right) + \frac{2}{R} J_{PM}, \quad (27)$$

$$J_{PM} = -J_P - J_N + J_{SYN} + J_{l,p}. \quad (28)$$

For the reduced model (herein referred to as the Borole et al. model), we have removed consideration of the endoplasmic reticulum and buffering ionic reactions. Note that this model is equivalent to our expanded flux model as $\Delta x, dR/dx \rightarrow 0$. In the plasma membrane flux term, J_{PM} , we have included: plasma membrane Ca^{2+} -ATPase (PMCA) pumps, J_P ; $\text{Na}^+/\text{Ca}^{2+}$ exchangers (NCX), J_N ;

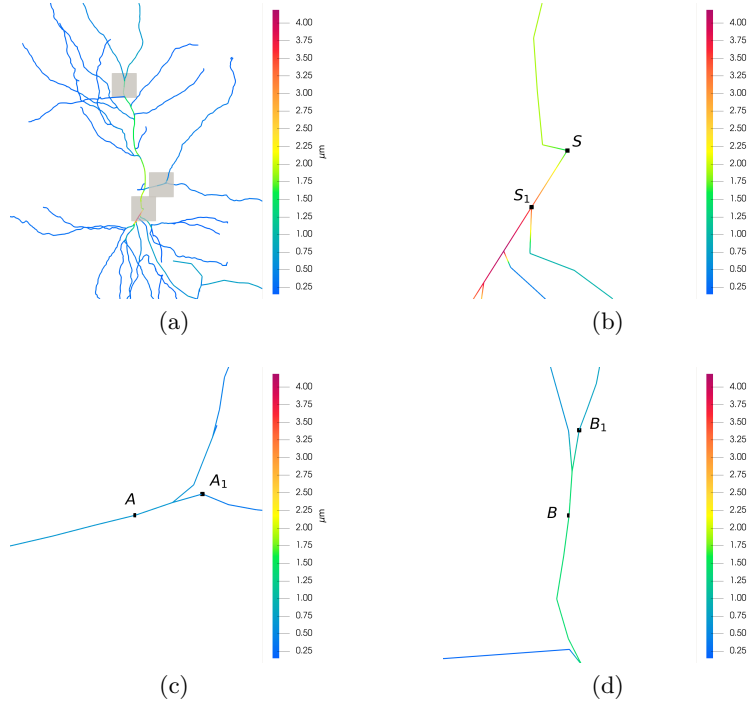


Figure 14: Nodes (S, A, B) and nearby nodes (S_1 , A_1 , B_1). (a) The complete neuronal model used with the radius indicated, and regions of each measuring node highlighted. (b)-(d) Zoom in of each highlighted region, detailing the region local to each measuring node and labels of node locations.

calcium influx through post-synaptic density, J_{SYN} ; and the leak calcium flux across the plasma membrane, $J_{l,p}$. Details of the complete mathematical models for each of the J_{PM} flux terms can be found in [6].

The complete neuronal geometry is shown in Fig. 14a. We select three nodes at which to provide a synaptic input: the soma (node S) and two branching nodes (nodes A and B). At each of these nodes, a 2 millisecond (ms) stimulus is applied every 10 ms, with the stimuli staggered by 0.5 ms (node S receives its first stimulus at 0 ms, node A at 0.5 ms, and node B at 1 ms). This periodic stimulus serves as a model for the effects of repetitive transcranial magnetic stimulation (rTMS) treatments on intracellular calcium dynamics. Additionally, we record the concentration at nearby nodes S_1 , A_1 , and B_1 , shown in Fig. 14b-14d, to compare the results of our model with the standard one in regions of large radial gradients.

In Fig. 14a, we show the radius of the dendrites of the neuron in the region of consideration. We see a large radius at the soma (near node S), and a quick decrease in radius at each branching point, particularly clear near node B. ($dR/dx|_S = 0.43$, $dR/dx|_A = -0.03$, $dR/dx|_B = -0.10$.) As will be demonstrated in this section, our expanded model computes significantly different concentrations in these regions in response to the changing radius.

When using a realistic geometry, satisfying stability conditions for the first order term is a significant obstacle. Central differencing is instead used for the first order term, which eases the requirements for stability. The same physical conservation considerations are taken at branching nodes as used in the derivation of the upwinding method. For additional stability in time stepping, a second order semi-implicit backward differentiation formula (SBDF2) is used [25].

In Fig. 15, we show the calcium concentration at each selected node using both the Borole et al.

model and our EF-FJ model. The most prominent difference can be seen at node S, where the soma has a very significant radial change from the dendrite. There is a very slight difference in nodes A and B, where there is a large change in the radius at the branching node but very little change through the rest of the dendrite. We see particularly at nearby nodes S_1 , A_1 , and B_1 , a significant difference in results after the steep change in radius through the soma or past the branching points.

The most drastic difference is clearly seen at Node S, where, even though the stimulus is applied in the same way for both models, the drastic change in radius gives much different quantitative behavior. Our EF-FJ model shows a concentration approaching a relatively stable oscillation quickly, while the Borole et al. model continues to increase. This further demonstrates that the radial gradient consideration in our model has a significant impact on results and can provide more accurate results without the need for expensive higher dimensional computation.

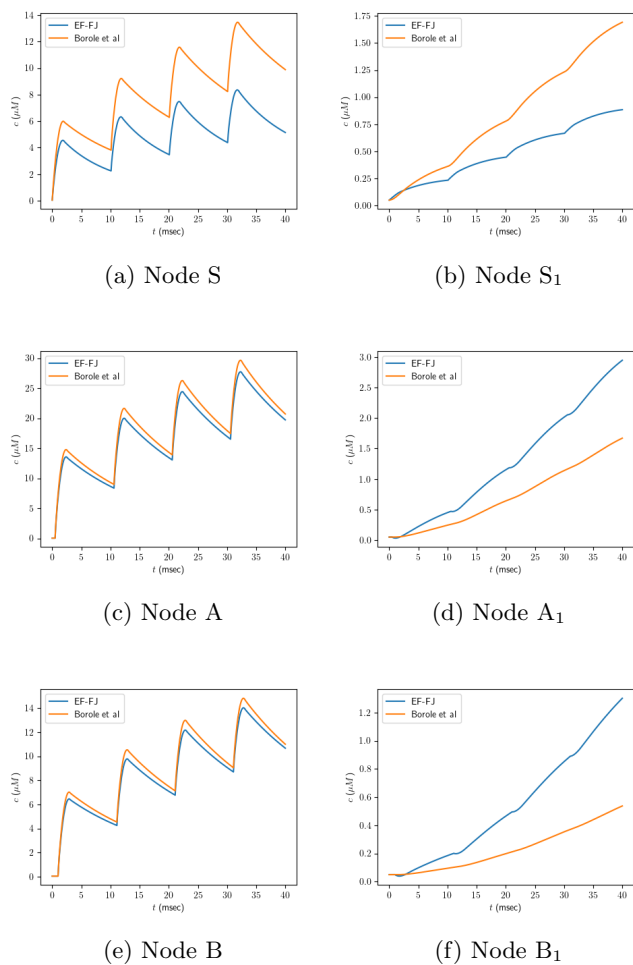


Figure 15: Concentration at each node (S, A, B) and nearby nodes (S_1 , A_1 , B_1) using the EF-FJ model vs. Borole et al. model.

6 Conclusion

In this paper, we have provided a new and simple derivation of the Fick-Jacobs equation that adds additional high order spatial derivative terms which provide better stability and accuracy in a computational setting than previous corrections. We derived simplified finite difference discretizations for branch points within networks, and established analytical stability conditions for these methods. Finally, we demonstrated the improved computational efficiency, stability, and accuracy of our method through computational examples of diffusion through channels and branches of varying radius.

Put together, we have established a computationally efficient and accurate dimension reduced model of diffusion through a network of porous channels. This has a wide array of applications in biology, engineering, and various other sciences. Our further interest lies specifically in neuroscience, where we aim to develop extended simulations of ion transport within neurons [10, 8, 7, 24, 27, 29, 6]. The dimension reduced model we have developed will help create long time simulations that give insight into the timescales relevant for clinical applications.

References

- [1] J. ALVAREZ-RAMIREZ, L. DAGDUG, L. INZUNZA, AND E. RODRIGUEZ, *Asymmetrical diffusion across a porous medium-homogeneous fluid interface*, Physica A: Statistical Mechanics and its Applications, 407 (2014), pp. 24–32.
- [2] A. BEREZHKOVSII AND G. HUMMER, *Single-file transport of water molecules through a carbon nanotube*, Phys. Rev. Lett., 89 (2002), p. 064503.
- [3] A. M. BEREZHKOVSII, L. DAGDUG, AND S. M. BEZRUKOV, *Range of applicability of modified Fick-Jacobs equation in two dimensions*, J. Chem. Phys., 143 (2015), p. 164102.
- [4] A. M. BEREZHKOVSII, M. A. PUSTOVOIT, AND S. M. BEZRUKOV, *Diffusion in a tube of varying cross section: Numerical study of reduction to effective one-dimensional description*, J. of Chem. Phys., 126 (2007), p. 134706.
- [5] P. BOROLE, *CalciumSim: Simulator for calcium dynamics on neuron graphs using dimensionally reduced model*, Master’s thesis, Temple University, Philadelphia, PA, 2022.
- [6] P. BOROLE, J. M. ROSADO, M. R. NEAL, AND G. QUEISSER, *Neuronal resilience and calcium signaling pathways in the context of synapse loss and calcium leaks: A computational modeling study and implications for Alzheimer’s disease*, SIAM J. on Appl. Math., 83 (2023), pp. 2418–2442.
- [7] M. BREIT AND G. QUEISSER, *What is required for neuronal calcium waves? a numerical parameter study*, The Journal of Mathematical Neuroscience, 8 (2018), pp. 1–22.
- [8] M. BREIT, M. STEPNIEWSKI, S. GREIN, P. GOTTMANN, L. REINHARDT, AND G. QUEISSER, *Anatomically detailed and large-scale simulations studying synapse loss and synchrony using neurobox*, Frontiers in Neuroanatomy, 10 (2016), p. 8.
- [9] G. CHACÓN-ACOSTA, A. LEÓN-RAMÍREZ, AND O. GONZÁLEZ-GAXIOLA, *Biharmonic Fick–Jacobs diffusion in narrow channels*, Physica A, 628 (2023), p. 129155.

- [10] S. GREIN, M. STEPNIIEWSKI, S. REITER, M. KNODEL, AND G. QUEISSER, *1d-3d hybrid modeling - from multi-compartment models to full resolution models in space and time*, *Frontiers in Neuroinformatics*, 8 (2014), p. 68.
- [11] Q. GUAN AND G. QUEISSER, *Modeling calcium dynamics in neurons with endoplasmic reticulum: Existence, uniqueness and an implicit–explicit finite element scheme*, *Comm. in Nonlinear Sci. and Num. Sim.*, 109 (2022), p. 106354.
- [12] A. GURUNG AND Q. GUAN, *Hybrid PDE-deep neural network model for calcium dynamics in neurons*, 2024.
- [13] B. HILLE, *Ion Channels of Excitable Membranes, 3rd ed.*, Sinauer Associates, Inc., Sunderland, Massachusetts, 2001.
- [14] M. HINES, *Efficient computation of branched nerve equations*, *Int. J. Bio-Medical Computing*, 15 (1984), pp. 69–76.
- [15] M. H. JACOBS, *Diffusion Processes*, Springer-Verlag, New York, 1967.
- [16] P. KALINAY, *When is the next extending of Fick-Jacobs equation necessary?*, *J. Chem. Phys.*, 139 (2013), p. 054116.
- [17] P. KALINAY AND J. K. PERCUS, *Corrections to the Fick-Jacobs equation*, *Phys. Rev. E*, 74 (2006), p. 041203.
- [18] U. F. KEYSER, B. N. KOELEMAN, S. VAN DORP, R. M. M. S. D. KRAPF, S. LEMAY, N. DEKKER, AND C. DEKKER, *Direct force measurements on DNA in a solid-state nanopore*, *Nat. Phys.*, 2 (2006), pp. 473–477.
- [19] D. P. LUCERO, *Performance characteristics of permeation tubes*, *Anal. Chem.*, 43 (1971), pp. 1744–1749.
- [20] Z. M. MIKSIS AND G. QUEISSER, *A physics-informed neural network for coupled calcium dynamics in a cable neuron*, in *ICLR 2024 Workshop on AI4DifferentialEquations in Science*, Vienna, AT, May 2024.
- [21] S. K. MITUSCH, S. W. FUNKE, AND M. KUCHTA, *Hybrid FEM-NN models: Combining artificial neural networks with the finite element method*, *J. Comp. Phys.*, 446 (2021), p. 110651.
- [22] D. REGUERA AND R. RUBÍ, *Kinetic equations for diffusion in the presence of entropic barriers*, *Phys. Rev. E*, 64 (2001), p. 061106.
- [23] J. M. ROMERO, O. GONZÁLEZ-GAXIOLA, AND G. CHACÓN-ACOSTA, *Exact solutions to Fick-Jacobs equation*, *Int. J. of Pure and Appl. Math.*, 82 (2013), pp. 41 – 52.
- [24] J. ROSADO, V. D. BUI, C. A. HAAS, J. BECK, G. QUEISSER, AND A. VLACHOS, *Calcium modeling of spine apparatus-containing human dendritic spines demonstrates an “all-or-nothing” communication switch between the spine head and dendrite*, *PLoS computational biology*, 18 (2022), p. e1010069.
- [25] B. SEIBOLD, D. SHIROKOFF, AND D. ZHOU, *Unconditional stability for multistep ImEx schemes: Practice*, *J. of Comput. Phys.*, 376 (2019), pp. 295–391.

- [26] Y. SHI, Y. T. LEE, AND A. S. KIM, *Knudsen diffusion through cylindrical tubes of varying radii: Theory and Monte Carlo simulations*, *Transport in Porous Media*, 93 (2012), pp. 517–541.
- [27] S. SHIRINPOUR, N. HANANEIA, J. ROSADO, H. TRAN, C. GALANIS, A. VLACHOS, P. JEDLICKA, G. QUEISSER, AND A. OPITZ, *Multi-scale modeling toolbox for single neuron and subcellular activity under transcranial magnetic stimulation*, *Brain Stimulation*, 14 (2021), pp. 1470–1482.
- [28] J. W. THOMAS, *Numerical Partial Differential Equations: Finite Difference Methods*, no. 22 in *Texts in Applied Mathematics*, Springer, 1995.
- [29] W. M. YAMADA, C. KOCH, AND P. R. ADAMS, *Multiple Channels and Calcium Dynamics*, Bradford Books, Toronto, ON, 1998, ch. 2, pp. 137–170.
- [30] R. ZWANZIG, *Diffusion past an entropy barrier*, *J. Phys. Chem.*, 96 (1992), pp. 3296 – 3930.